

VICTORIA UNIVERSITY
MELBOURNE AUSTRALIA

Performance of asymmetric hollow fibre membranes in membrane distillation under various configurations and vacuum enhancement

This is the Published version of the following publication

Zhang, Jianhua, Li, Jun-de, Duke, Mikel, Xie, Zongli and Gray, Stephen (2010) Performance of asymmetric hollow fibre membranes in membrane distillation under various configurations and vacuum enhancement. *Journal of Membrane Science*, 362 (1-2). pp. 517-528. ISSN 0376-7388

The publisher's official version can be found at
<http://dx.doi.org/10.1016/j.memsci.2010.07.004>
Note that access to this version may require subscription.

Downloaded from VU Research Repository <https://vuir.vu.edu.au/15836/>

Performance of asymmetric hollow fibre membranes in membrane distillation under various configurations and vacuum enhancement

Jianhua Zhang¹, Jun-De Li¹, Mikel Duke¹, Zongli Xie^{1,2}, Stephen Gray^{1*}

1 Institute of Sustainability and Innovation, Victoria University, PO Box 14428, Melbourne, Victoria 8001, Australia (E-mail: stephen.gray@vu.edu.au)*

2 CSIRO Materials Science & Engineering, PO Box 33, Clayton, Vic. 3169, Australia

Abstract

Hollow fibre membrane distillation (MD) modules have a more compact structure than flat sheet membrane modules, providing potentially greater advantage in commercial applications. In this paper, a high-flux asymmetrically-structured hollow fibre MD module was tested under various conditions. The results show that increasing velocity and temperature are positive for flux, and salt rejection was more than 99% over the entire experimental range. The hollow fibre module also showed great variation in flux when altering the hot feed flow from the lumen side to the shell side of the fibre, and this phenomenon was analysed based on the characterisation of the asymmetric structure of the hollow fibre. The largest mass transfer resistance was determined to be in the small pore size skin layer on the outer surface of the membrane, and having the hot feed closest to this surface provided the greatest vapour pressure difference across this high resistance mass transfer layer. The results also show that placing the suction pump on the permeate outlet increased the flux by lowering the pressure within the pore and hence increased the rate of vapour mass diffusion. A maximum flux of $19 \text{ Lm}^{-2}\text{h}^{-1}$ was obtained at 85°C when hot feed was entering the shell side, and the mass transfer coefficient was relatively constant across the entire temperature range when operated at high velocities. These outcomes suggest that asymmetric hollow fibre MD modules should be operated with hot brine feed closest to the high resistant skin layer, and that vacuum enhanced MD further increases vapour transport and flux.

Keywords

Membrane distillation; hollow fibre; desalination; direct contact membrane distillation; vacuum enhanced direct contact membrane distillation

1. Introduction

Membrane distillation is a developing technique for desalination. Its driving force is a vapour pressure difference across a membrane, which is quite different from other membrane processes in which an absolute pressure difference, a concentration gradient or electrical potential gradients are the driving force for mass transfer. It has 100% theoretical rejection of non-volatile components and can utilise low grade heat sources of $40\text{-}80^\circ\text{C}$. Its flux is not sensitive to salt concentration in the feed, since vapour pressure is not greatly affected by the salinities found in practical water treatment. Thus, it is a potential commercial desalination technique if it can be combined with solar energy, geothermal energy or waste heat available in power stations or chemical plants. It could also be an effective method to reduce the volume of waste discharges or even convert a reject stream to a higher value concentrated liquid. Therefore, MD can be combined with conventional reverse osmosis processes to minimise high concentration brine discharge.

Figure 1 shows a tubular hollow fibre module (a) and a flat sheet module (b), which are the most popular configurations employed for membrane distillation. In comparison with the flat sheet module, the hollow fibre module has larger effective area per unit volume.

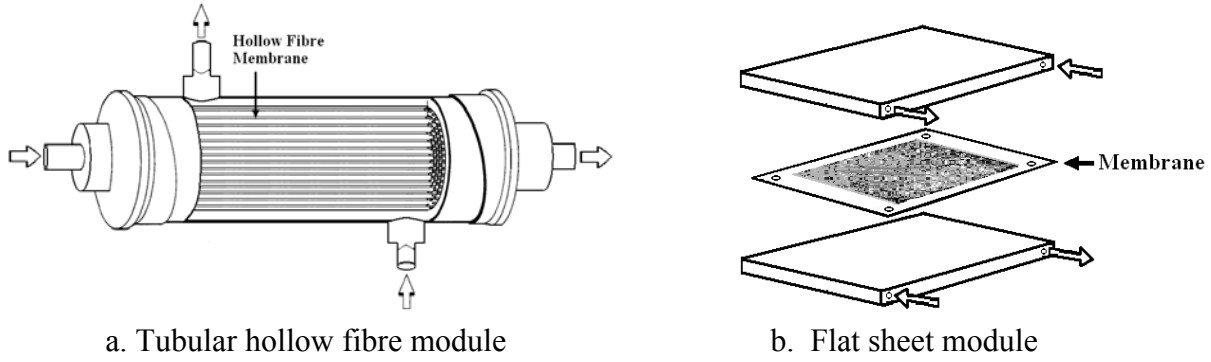


Figure 1: Configurations of MD module

In the MD process, the force preventing process liquid wetting the membrane pores results from both the hydrophobicity of membrane material and the liquid surface tension. The lowest wetting pressure, the Liquid Entry Pressure (LEP) [1] can be calculated from

$$LEP = \frac{-2B\gamma_l \cos \theta}{r_{max}} \quad (1)$$

where B is a geometric factor, γ_l is the surface tension of the solution, θ is the contact angle between the solution and the membrane surface, and r_{max} is the largest membrane pore size. If the maximum pore size of membrane is $1 \mu\text{m}$ [2], the LEPs of membranes with the contact angles of 95° and 140° calculated from Eq. (1) are 23 and 204 kPa respectively, which would be the upper application pressure limits of such membranes. These calculations demonstrate the large effect that contact angle of the membrane has on the LEP, and subsequently on the maximum operating pressures and velocities in MD modules. In a commercial application, the effective membrane area will be tens or hundreds of times of that of laboratory scale tests, and a reasonable flow velocity needs to be maintained to reduce temperature polarisation [3]. Therefore, to avoid wetting, the hydrophobicity of membrane material and hydraulic resistance of the module with turbulence enhancing structure will be very important for commercial design. From Figure 1, we observe that it is easier to put more effective area into the hollow fibre module with less restriction than that of the flat sheet module, however, turbulence promoters are likely to be required to reduce temperature polarisation.

One of the main impediments of the hollow fibre module is its typically low flux, which is generally $1\text{-}4 \text{ L}\cdot\text{m}^{-2}\cdot\text{h}^{-1}$ at $40\text{-}60^\circ\text{C}$ [4-6]. This is much lower than that of the flat sheet membranes with fluxes of $20\text{-}30 \text{ L}\cdot\text{m}^{-2}\cdot\text{h}^{-1}$ [7]. However, the recent renewed interest in membrane distillation has led to improved hollow fibre membranes and modules.

1.1 Force balance analysis at pore entrance

Figure 2 shows the force balance at the entrance of pore, in which P_f and P_p are respectively the gauge pressure of the feed flow and permeate flow, P is the total gauge pressure in the pore, F is the force from surface tension, H is the water protrusion into the pore and θ' is the angle between the water and membrane material. Additionally, θ' can not be more than θ before wetting, and the initial P equals zero gauge pressure (atmospheric pressure).

In considering Figure 2, it can be speculated that the pressure in the pore will remain almost constant, assuming the membrane material is not compressible. When P_f and/or P_p are higher than zero and increasing in value relative to P , the depth of protrusion will also increase (H and θ' will become greater to balance the increased liquid pressure). When either feed or permeate pressure is less than zero, the higher pressure in the pore will cause air to bubble into the lower pressure liquid,

until P equals this lower pressure. Furthermore, assuming a membrane with pore size of $1\ \mu\text{m}$ and contact angle of 150° , based on Eq. (1) the maximum protrusion H is $0.3\ \mu\text{m}$. When considering a typical membrane thickness of $10\text{-}50\ \mu\text{m}$, this protrusion will have a negligible effect on the air volume within the pore.

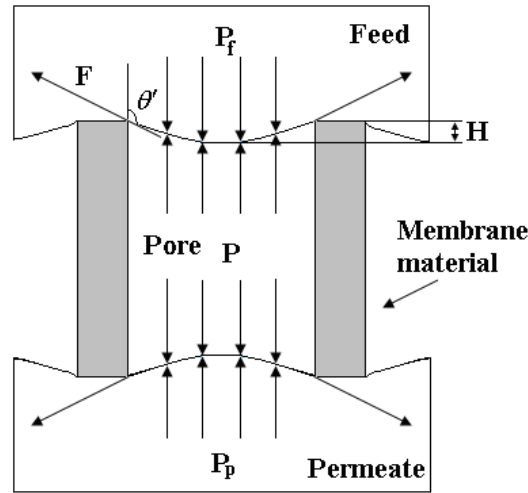


Figure 2. Schematic of force balance in the pore

1.2 Mass transfer in DCMD

Figure 3 shows the heat and mass transfer processes in direct contact membrane distillation (DCMD). The liquid feed and cooling flow are not in contact with each other, but are physically separated by the membrane and gas trapped within the pores. The feed temperature, T_f drops across the feed side boundary layer to T_l , as water evaporates and is transported through the membrane and heat is conducted through the membrane to the permeate side. The permeate temperature, T_p , increases across the permeate boundary layer to T_2 as the permeate flow condenses into the fresh water stream and gains heat from the feed side. The real driving force is therefore, the vapour pressure difference between T_l and T_2 , which is less than the vapour pressure difference between T_f and T_p . This phenomenon is called temperature polarisation.

The hydrophobic MD membrane is a porous medium. The mass transfer through such medium can be interpreted by three kinds of basic mechanisms: Knudsen diffusion, molecular diffusion and Poiseuille flow. Knudsen number (Kn) shown in Eq. (2), is used to judge the dominating mechanism of the mass transfer in the pore.

$$Kn = \kappa / d \quad (2)$$

Here, κ is the mean free path of the transferred gas molecule and d is the mean pore diameter of the membrane.

Table 1 shows the dominating mass transfer mechanism based on the Kn in a gas mixture system without a total pressure difference [8].

Table 1
Mass transfer mechanism in membrane pore

$Kn < 0.01$	$0.01 < Kn < 1$	$Kn > 1$
molecular diffusion	Knudsen-molecular diffusion transition mechanism	Knudsen mechanism

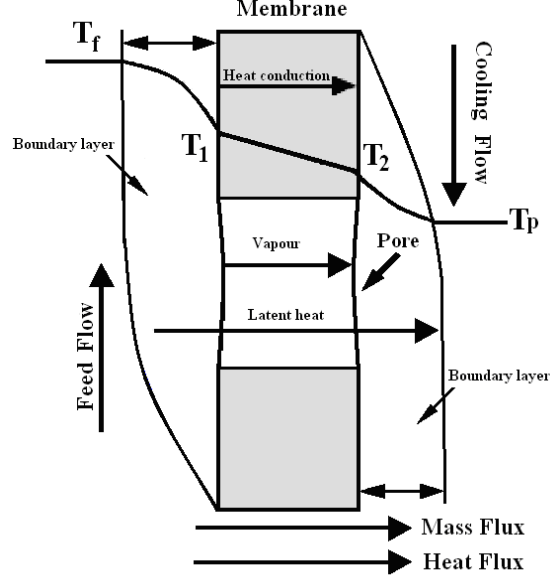


Figure 3. Heat transfer and mass transfer through membrane

Mass transfer in the DCMD process, assuming convective heat transfer in the liquid phase, includes five main steps. These are: water molecules diffuse from the bulk feed into the boundary layer, vaporise from liquid/gas interface of the feed, pass through the membrane pores, condense at the liquid/gas interface of the permeate side, and diffuse into the bulk permeate.

The mass transfer model of membrane distillation assumes that the mass transfer rate or water flux is proportional to the vapour pressure difference across the membrane [9] represented in Eq. (3).

$$N = C_{membrane} (P_{T_1} - P_{T_2}) = C_{global} (P_{T_f} - P_{T_p}) \quad (3)$$

Here, $C_{membrane}$ is the membrane mass transfer coefficient which depends only on the membrane properties and gas conditions within the pore, P_{T_1} and P_{T_2} are the vapour pressures at T_1 and T_2 , respectively, C_{global} is the global mass transfer coefficient which involves both boundary layer effects and membrane effects. As there is an exponential relationship between temperature and vapour pressure, Eq. (3) predicts that permeate flux N is an exponential function of temperature. $C_{membrane}$ is an important parameter to assess membrane performance and depends on the characteristics of the membrane as given [8],

$$C_{membrane} \propto \frac{r^a \varepsilon}{bt} \quad (4)$$

Here, r is the nominal pore size of the membrane, ε is the membrane porosity, a is a coefficient in the range of 1 to 2, b is the membrane thickness and t is pore tortuosity.

However, it is difficult to determine $C_{membrane}$ experimentally, because T_1 and T_2 are difficult to measure. Thus, C_{global} is often used to assess process performance, which includes the mass transfer phenomena in the boundary layer.

1.3 Heat transfer

The heat transfer in DCMD is combined with simultaneous mass transfers, which are in the same direction from the feed side to the permeate side. Assuming no heat loss through module walls, the total heat flux can be expressed as [4, 10, 11]:

$$Q = \alpha_1 (T_f - T_1) = H_{latent} N + \frac{2\lambda}{d_o \ln(d_o / d_i)} (T_1 - T_2) = \alpha_2 (T_2 - T_p) \quad (5)$$

where α_1 and α_2 are the heat transfer coefficients on hot side and cold side respectively, λ is the thermal conductivity of the membrane, N is the vapour flux through the membrane and H_{latent} is the latent heat of vaporisation for water, d_i and d_o are the inner and outer diameters of the hollow fibre, In Eq. (5), $2\lambda(T_1-T_2)/(d_o \ln(d_o/d_i))$ is the sensible heat transfer across the membrane and $H_{latent}N$ is the latent heat transfer resulting from mass transport. The thermal conductivity λ can be calculated as [4, 10]

$$\lambda = (1 - \varepsilon)\lambda_{solid} + \varepsilon\lambda_{air} \quad (6)$$

where λ_{solid} and λ_{air} are thermal conductivities of air and solid respectively

In this paper, a high-flux asymmetrically-structured hollow fibre module was tested and its structure used to explain flux variations resulting from changes in MD configuration.

2. Experimental methods

2.1 Hollow fibre membrane and module

Table 2 lists the characteristics of the membranes as specified by the supplier and the dimension of the module used in the experiments. The membranes were composed of a fluorinated hydrocarbon.

Table 2
Nominal specifications of hollow fibre membranes

Inner module diameter (mm)	Effective length (m)	Number of fibres	Nominal pore size (μm)
25	0.51	94	0.3

2.2 Characterisation of hollow fibre membrane

2.2.1 Hollow fibre membrane dimensions

The hollow fibre was frozen in liquid nitrogen and then cut to form a smooth and intact cross section. The inner and outer diameters were measured by taking photograph of the fibre cross section along side a millimetre scale reference. Measurement was taken for 5 fibre pieces and the mean value was used to calculate the effective area.

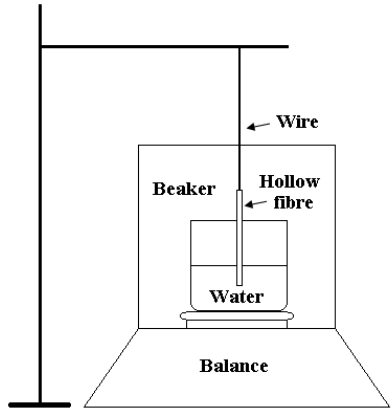
2.2.2 Contact angle measurement

Contact angles of inner and outer surfaces were measured via surface tension effects based on [12],

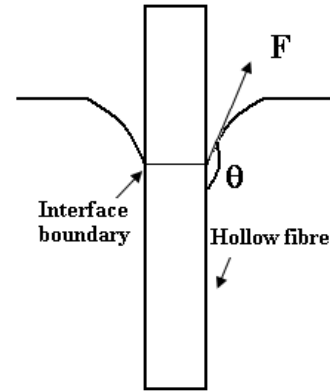
$$F = \pi d_o \gamma_l \quad (7)$$

$$h = \frac{-4\gamma_l \cos \theta}{\rho g d_i} \quad (8)$$

where ρ is water density, h is the height between the water protrusion and water surface in the beaker and g is acceleration due to gravity.

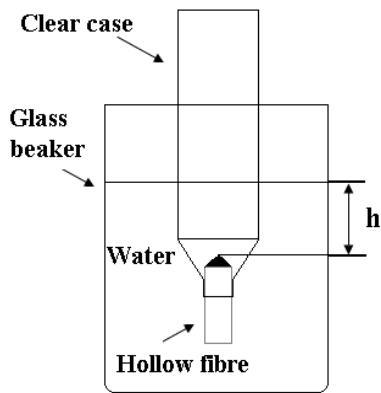


a. Measurement schematic for outer surface

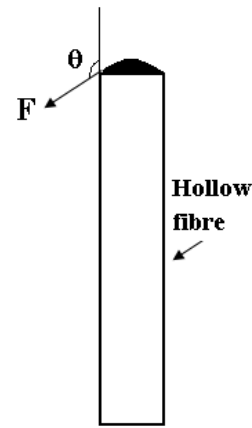


b. Force balance at interface boundary

Figure 4. Contact angle measurement for outer surface



a. Measurement schematic for inner surface



b. Force balance at interface boundary

Figure 5. Contact angle measurement for inner and outer surfaces

Figures 4 and 5 show schematic diagrams of the measurement and force balance at the interface boundary. For the contact angle measurement of the outer surface, part of the fibre was submerged into the water and the mass changed with time recorded, allowing the mass reduction arising from surface tension effects to be determined. Assuming the evaporation rate is constant at room temperature (20°C), the intercept of the change in mass with time ($t=0$ when the fibre is immersed in water) is the mass reduction resulting from the surface tension, F , which can be calculated from Eq. (7). From Figure 4b [12], it can be deduced that,

$$\Delta m = F \cos \theta \quad (9)$$

where Δm is the mass difference arising from F . From this, we can obtain

$$\theta = \cos^{-1} \left(\frac{\Delta m}{F} \right) \quad (10)$$

For the contact angle measurement of the inner surface, part of the hollow fibre was encased in a clear cylinder, and high vacuum grease used to seal the clearance between the fibre and the cylinder. The fibre was slowly submerged into the water and the height difference (h) between the top of the fibre and water surface recorded when water first protruded from the top of the fibre. The experiments were repeated four times. According to Eq. (8), the contact angle can be determined from

$$\theta = \cos^{-1}\left(-\frac{h\rho g d_i}{4\gamma_l}\right) \quad (11)$$

2.2.3 Porosity measurement

The porosity was measured by the wetting method [13]. To reduce the error, eight fibres with a total calculated volume of 4.2 ml (based on the mean ID and OD) were used. According to the wettability of the fibre material, the total unwetted fibre volume (including pore volume) and the total wetted fibre volume (mass volume) were measured by soaking the fibre in deionised water and ethanol. The porosity was calculated by

$$\varepsilon = 1 - \frac{V_{mass}}{V_{total}} \quad (12)$$

where the V_{mass} is the mass volume and V_{total} is the total fibre volume.

2.2.4 Pore distribution and pore size measurement

Both pore size distribution and mean pore size were measured by a BET (Micromeritics TriStar 3000) instrument using nitrogen gas in cell immersed in boiling liquid nitrogen (77K). Pore size and pore size distribution were calculated from the BJH absorption result. To avoid polymeric material degradation during degassing, the hollow fibre was degassed at a temperature of 70°C for 48 h.

2.2.5 SEM characterisation

Surface and cross sectional structures were observed by a Philips XL30 FEG Scanning Electron Microscope (SEM) to verify the results from BET. The investigated membrane was fractured following immersion in liquid nitrogen to form an intact cross section.

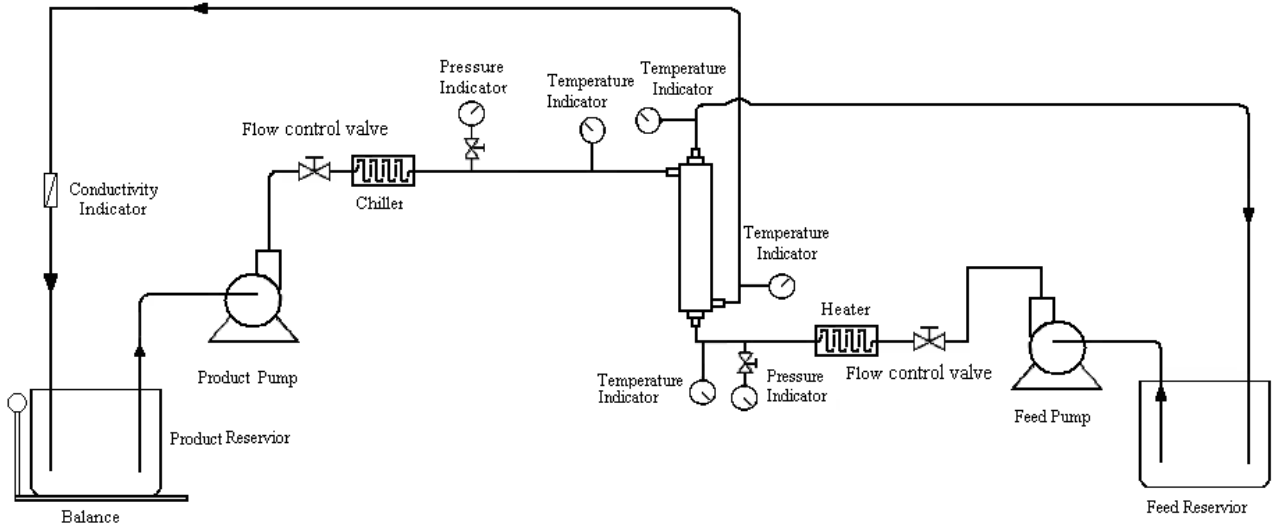
2.3 DCMD and VEDCMD Testing

Three experimental configurations were used in the experiments. Figure 6 shows a schematic diagram of Setup I, in which the hot feed passed through the lumen side of the hollow fibres and the cold flow passed through the shell side (outside the lumen) of the module. Velocities were controlled by two pumps, one for the hot feed and the other for the cold flow. The feed velocities were varied in the range of 0.24-1.7 m/s (1-7 L/min) and 0.23-0.60 m/s (4-10.4 L/min) respectively in Setup I and II. The feed temperature was controlled by a digitally controlled heater and was varied in the range of 30-90°C. A digitally controlled refrigerated water bath was used to control the temperature of the cold flow so that it could be recirculated at constant temperature. The temperature for the cold stream inlet was set at 20°C. The brine feed was prepared by dissolving 100 g NaCl in 10 L water (10 g.L⁻¹). Four temperature sensors were used to measure the temperatures of the hot brine and cold flow sides at their respective inlets and outlets. Two pressures sensors were placed upstream of the hot feed and permeate entrances to monitor the pressure of each side. A conductivity meter in the product reservoir was used to monitor changes which were used to calculate salt rejection. Flux was determined by measuring the weight of the product reservoir over time and was calculated based on the outside membrane area. All flux results presented were measured based on the outer surface area over a period of 3 to 8 hours and variation in flux over this time was ±5%.

The two variations of Setup I included swapping the flow paths of the hot feed flow and the cold

1 flow (Setup II; hot feed through the shell side and cold flow through the lumen), and moving the
 2 cold flow pump downstream to draw the cold flow through the module (Setup III; hot feed through
 3 the lumen and cold flow through the shell side).

4 Although no noticeable flux decay was found in these experiments, after every series of
 5 experiments, the membrane was cleaned by fully wetting with ethanol and soaking in 0.1 mol/L
 6 HCl solution for 3-10 min.



8
 9 Figure 6. Schematic diagram of the experimental setup

10
 11
 12 **3. Results**

13
 14 *3.1 Membrane properties*

15
 16 Table 3 lists the measured and calculated properties of the membrane.

17
 18 Table 3
 19 Measured and calculated properties of membrane

Mean fibre diameter (mm)		Membrane thickness (mm)	Mean effective area (m ² /module)		Mean pore size (μm)	Surface contact angle		Mean porosity (%)
Inner	Outer		Inner	Outer		Inner	Outer	
0.94	1.67	0.73	0.15	0.24	0.33	126±3°	94±2°	81.0

20
 21 The membrane was less hydrophobic than Teflon membranes [14] based on the measured contact
 22 angle, while the mean pore size acquired from BET was similar to the provided data in Table 2.

23 The porosity of the hollow fibre was 81%, which was higher than that of polypropylene hollow
 24 fibre membrane (75% porosity) used for membrane distillation and other applications [15, 16],
 25 lower than MD polyvinylidene fluoride (PVDF) MD membrane (~85% porosity) [17, 18], and
 26 similar to the reported (PVDF) MD membrane loaded with 30% polytetrafluoroethylene (PTFE)
 27 [18].

28 In Figure 7, the SEM images show the structure of principal and skin layers. The inner and outer
 29 surface structures are shown in images 7a and 7b, in which it can be seen that the outer surface is
 30 smoother than the inner surface. Image 7c shows the structures of the cross section of the hollow
 31 fibre, which consists of a rough porous principal layer (7d) and a smooth dense skin layer with tiny
 32 pores (7e). From SEM image 7c, we estimated the skin layer to be 5 μm thick, which represents
 33 only 0.7% of the total membrane thickness (Table 3). In comparison with a symmetric membrane,

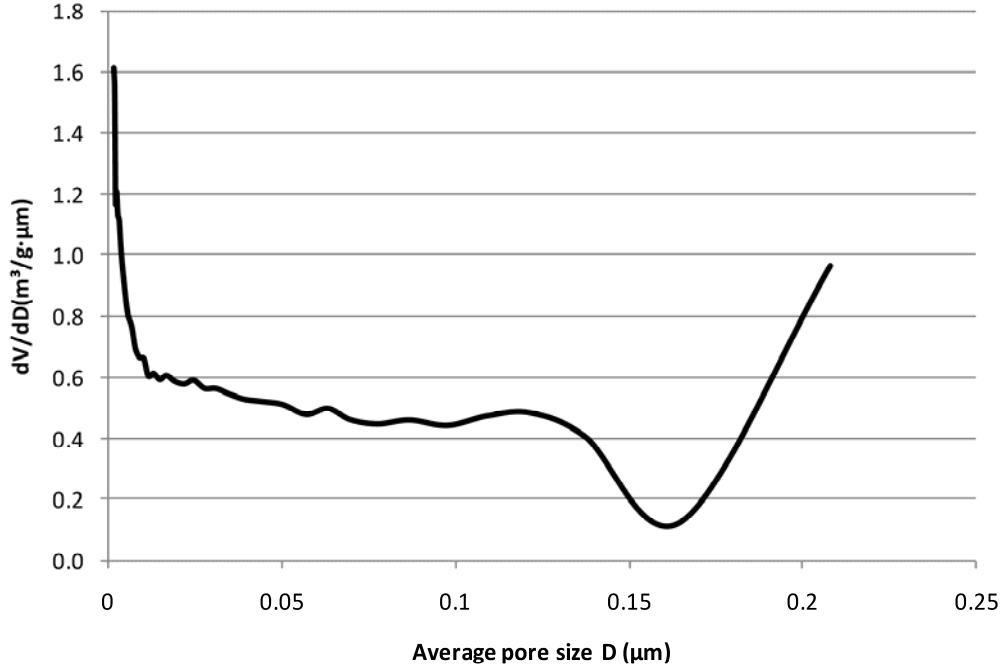


Figure 8. BJH membrane pore size distribution

3.2 Experimental results

3.2.1 Fluxes and global mass transfer coefficients at different velocities

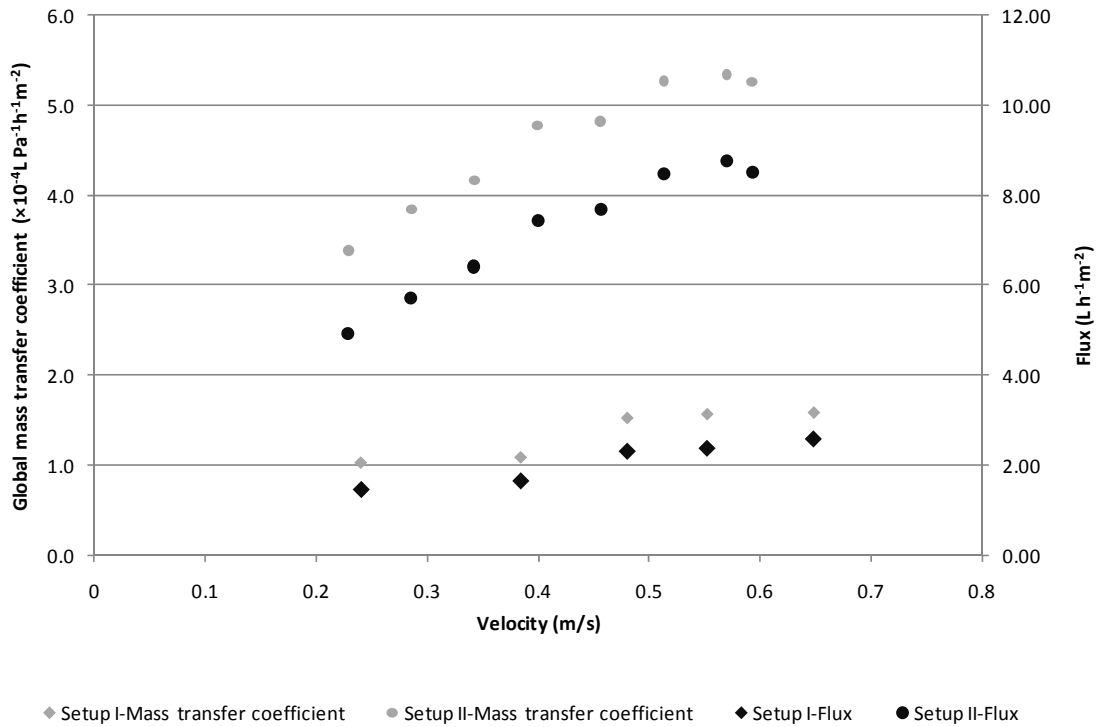
Variation of fluxes with velocities for Setup I and II are shown in Figure 9. In the experiments, inlet temperatures of the cold and hot sides were kept constant and controlled at 20°C and 60°C respectively. The volumetric flowrate on the hot and cold sides were identical, and the feed flowrate was varied in the range of 1-2.7 L/min (0.24-0.64 m/s) and 4-10.4 L/min (0.23-0.60 m/s) in Setup I and II respectively. When the velocity was increased, both the thermal and hydrodynamic boundary layers were thinned and temperature polarisation reduced because of greater turbulence [3]. As a result, the flux increased by 73% (from 1.5 to 2.6 L.m⁻²h⁻¹) for Setup I and 80% for Setup II (from 4.9 to 8.8 L.m⁻²h⁻¹). However, the increased velocity also reduced the residence time of the streams in the module. Therefore, the temperature difference between the hot brine and permeate streams also rose, because of the shortened mass and heat exchange time for a given volume of feed. Thus, the increased flux not only occurred from thinned boundary layers, but also from the increased temperature difference across the membrane. To assess the influence of increased turbulence more precisely, a global mass transfer coefficient, C_{global} , shown in Figure 9 was calculated using Eq. (3). The ΔP_{avg} was calculated from

$$\Delta P_{avg} = \frac{(P_{fi} - P_{po}) - (P_{fo} - P_{pi})}{\ln[(P_{fi} - P_{po}) / (P_{fo} - P_{pi})]} \quad (13)$$

where P_{fi} , P_{fo} , P_{pi} and P_{po} are the vapour pressures respectively at inlet and outlet temperatures of the hot side and cold side.

In Figure 9, both flux and global mass transfer coefficient curves show similar trends and become flatter at higher velocities. A similar asymptotic trend of permeate flux with increasing flow rates was reported previously [21, 22]. However, the global mass transfer coefficient increased by 53% (Setup I) and 58% (Setup II) with increasing velocity, which is less than the percentage increase of flux. In the higher velocity range, e.g. when velocity increased from 0.50 to 0.65 m/s, there were only 4% (Setup I) and 1.3% (Setup II) increases of global mass transfer coefficient, compared with

1 12.8% (Setup I) and 3.2% (Setup II) flux increase over the entire range of velocities. Therefore, at
 2 high velocities (the flattened part of the flux vs velocity curve), the increased flux resulted largely
 3 from the greater temperature difference across the membrane rather than that from greater
 4 turbulence, because the mass transfer coefficient, which accounts for temperature changes in bulk
 5 liquid, was close to constant. This is consistent with the boundary layer thickness being less
 6 sensitive to flow velocity at high velocities [23].



7 **Figure 9** Influence of velocity on flux and global mass transfer coefficient (Feed temperature 60°C
 8 permeate temperature 20°C)
 9

10 3.2.2 Temperature influence on membrane flux

11
 12 The fluxes as a function of hot side inlet temperatures (29-90°C) for Setup I and II are shown in
 13 Figure 10. The cold side inlet temperature was set at 20°C. The feed velocity was selected in the
 14 flattened part of the curves in Figure 9 to reduce the effect of the boundary layer on flux and
 15 remained constant at 1.7 m/s (7 L/min) for Setup I and 0.4 m/s (7 L/min) for Setup II. Fluxes for
 16 both setups showed an exponential relationship with the temperature, consistent with the increase in
 17 vapour pressure with temperature. Setup II had higher flux than that of Setup I for all temperatures
 18 across the entire temperature range, and the highest flux of 19.2 L.m⁻².h⁻¹ was observed at 86°C for
 19 Setup II.
 20

21 The global mass transfer coefficient shown in Figure 10 decreased slightly when the temperature
 22 rose, suggesting increased polarisation at higher temperatures [24].
 23

24 However, the variation of global mass transfer coefficient with temperature is not as great as its
 25 variation with velocity. The global mass transfer coefficient varied around the average by -12% to
 26 11% in Setup I and by -7% to 5% in Setup II at different temperatures, while for different velocities
 27 it is varied between -44% to 26% in Setup I and between -70% to 38% in Setup II.

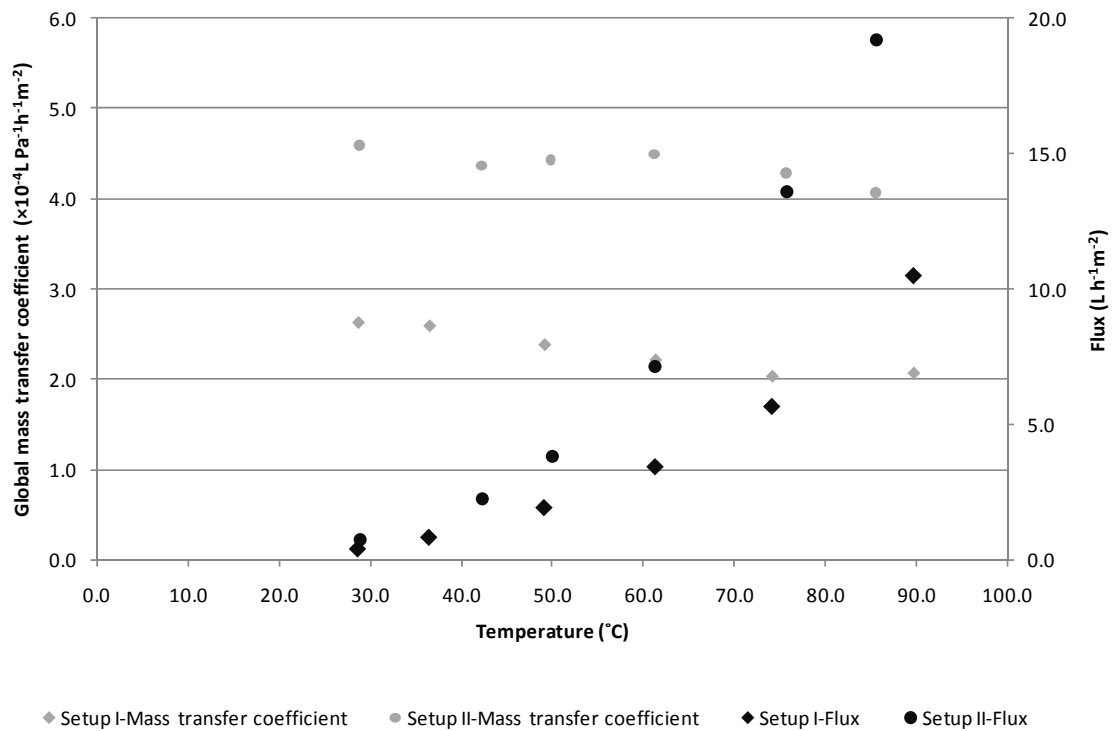
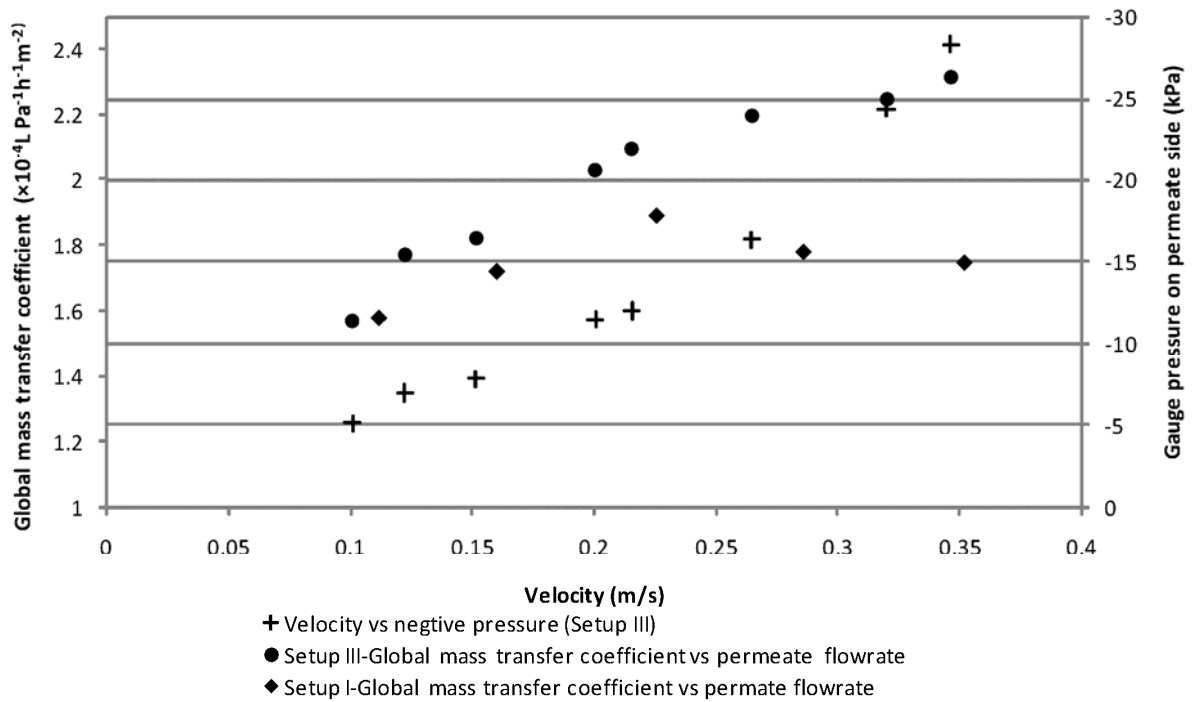


Figure 10 Flux and global mass transfer coefficient affected by temperature (Setup I - Feed velocity 1.7 m/s, Setup II - Feed velocity 0.4 m/s)

3.2.3 Flux variation with enhanced vacuum on the cold side

Vacuum enhanced direct contact membrane distillation (VEDCMD) employed in Setup III was used to test the effect of negative pressure on flux. To avoid damaging the membrane under conditions of reduced pressure, the cold flow was put under negative pressure from the shell side. For comparison purposes, the experiment was also conducted in Setup I. The hot feed velocity was kept constant at 1.7 m/s (7 L/min), cold permeate velocity was varied in the range of 0.1-0.35 m/s (1.6-2.3 L/min), and inlet temperatures on the hot and cold sides were set at 60 and 20°C, respectively. Figure 11 shows the effect of cold side velocity on global mass transfer coefficient and cold side pressure in both Setup I and III. With increasing cold stream velocity, the global mass transfer coefficient from Setup I increased initially, reached a maximum value at a feed velocity of 0.23 m/s, and then decreased. However, the global mass transfer coefficient obtained from Setup III increased with increasing velocity (lowered negative pressure) over the entire test range, and the slope reduced at higher vacuum pressures.



1
2 Figure 11. Vacuum enhanced membrane distillation (feed on lumen side, feed temperature 60°C,
3 permeate temperature 20°C)

4
5 *3.2.4 Feed pressure and salt rejection*

6
7 Salt rejection in all experiments was higher than 99% and did not change appreciably with the
8 velocity and temperature, which may be attributed to the large ID and the small pore size of the
9 hollow fibre membrane. In Figure 12, the relation between the inlet pressures on both sides of the
10 membrane and the flow velocity is presented. Even when the linear velocity on the lumen side was
11 as high as 2.5 m/s (10 L/min), the inlet pressure was only 90 kPa. This is still lower than the LEP of
12 a membrane with a maximum pore size of 1.7 μm calculated from Eq. (1), assuming B equals 1, γ_l is
13 the surface tension at 60°C, and θ is the contact angle ($126^\circ \pm 3$) of the inside surface.

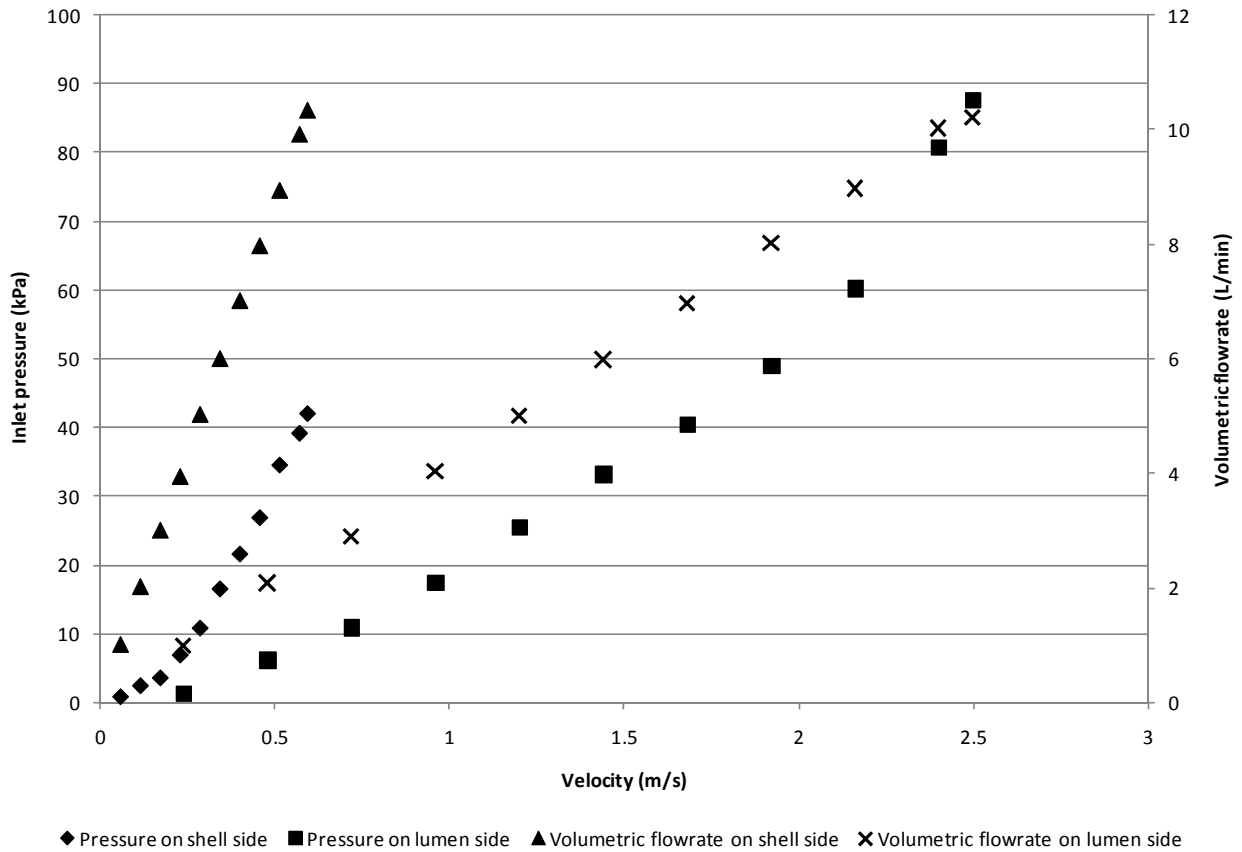


Figure 12 Relationship between inlet pressure and velocity (Setup I and II)

4. Discussion

For estimating purposes, the assumed parameters based on the BJH analytical results are listed in Table 4.

Table 4

Assumed parameters of the hollow fibre layers

<i>t</i>	Cumulative pore volumes (cm ³ /g)		Pore size (μm)		Thickness (μm)	
	Skin layer (1.7 ≤ D ≤ 1.9 nm)	Principle layer (0.15 ≤ D ≤ 0.23 μm)	Skin layer	Principle layer	Skin layer	Principle layer
1	0.0004	0.04	0.0018	0.33	5	725

In Table 4, the pore size of the skin layer was calculated from

$$r = 4V_{skin} / A_{skin} \quad (14)$$

where A_{skin} is the cumulative pore surface area for pores in size ranges of the skin layer.

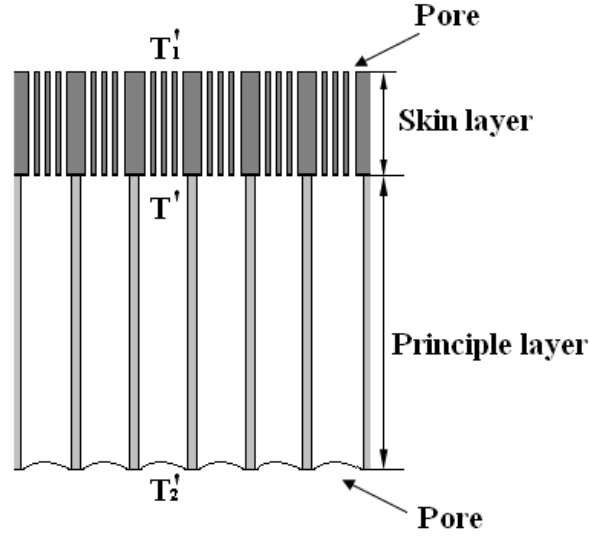


Figure 13 Schematic of the membrane structure and temperature distribution

Figure 13 shows a schematic diagram of the membrane structure, which consists of a thin skin layer and a thick principle layer. Here, T_1' is the interface temperature between the skin layer and the stream it is contacted with, T' is the temperature between the skin layer and principle layer, and T_2' is the interface temperature between the principle layer and the stream it is contacted with.

4.1 Vacuum enhanced membrane distillation

The observation of global mass transfer coefficient increasing with the decreasing pressure on permeate were also found in [25-27] and can be explained by the diffusion theory. Under the experimental conditions, the pore sizes of the principle layer and skin layer are estimated as 0.33 and 0.0018 μm and the mean free path of water vapour is 0.11 μm at feed temperature of 60°C [2], Kn calculated from Eq. (2) is 0.33 in the principle layer and 61 in the skin layer. Thus, in this experiment, the transport of water vapour through the principle layer can be interpreted by the Knudsen-molecular diffusion transition mechanism and the Knudsen mechanism in the skin layer [2, 28], and the flux can be described by:

$$N_k = \frac{8}{3} r \frac{\varepsilon}{b \cdot t} \sqrt{\frac{1}{2\pi RMT}} \Delta P \quad (15)$$

$$N_m = \frac{1}{1-x_A} \frac{\varepsilon D_{AB}}{b \cdot t RT} \Delta P \quad (16)$$

Because diffusivity in the pores can be described by:

$$D_{AB} = \frac{1.895 \times 10^{-5} T^{2.072}}{P} \quad (17)$$

and assuming it is an ideal gas mixture,

$$x_A = \frac{P_A}{P} \quad (18)$$

We derived,

$$N_m = \frac{1.895 \times 10^{-5} T^{1.072} \varepsilon}{b \cdot t R (P - P_A)} \Delta P \quad (19)$$

where N_k and N_m are fluxes contributed respectively by Knudsen and molecule diffusion transition mechanisms, R is universal gas constant, T is mean temperature in the pore, M is the molecular weight of water, ΔP is pressure difference across the membrane layer, x_A and P_A are mole fraction and partial pressure of water vapour in the pore and D_{AB} is the diffusivity of water vapour (A)

1 relative to air (B).

2 As depicted in Figure 2, when the permeate pressure is lower than the total pressure in the pore,
 3 the air in the pore will bubble out until the pressures in the pore and the low pressure side are again
 4 balanced. Therefore, if the permeate pressure decreases, the total pressure in the pore will decrease.
 5 From Eqs. (15)-(19), we find that N_k is a function of temperature and vapour pressure, and N_m is a
 6 function of temperature, vapour pressure and total pressure in the pore. Because the vapour pressure
 7 will only change with temperature under the experimental pressures shown in Figure 12, N_k will not
 8 be affected by the pressure decrease on the permeate side. However, N_m as represented in Eq. (19)
 9 will increase as the total pressure in the pore reduces with decreasing permeate pressure. Thus, in
 10 VEDCMD, the increase of global mass transfer results from a faster molecular transfer mechanism
 11 under lower pore pressure.

12 4.2 Influence of asymmetric structure of hollow fibre membrane on flux

13 4.2.1 Mass transfer resistance analysis

14
 15
 16
 17 The experimental results show that the flux of the hollow fibre module was not only affected by
 18 the temperature, velocity and negative pressure as generally accepted for membrane distillation [7],
 19 but also by the channel that the hot feed flowed through. This is seen in Figure 9, where flux from
 20 Setup II is nearly four times of that from Setup I under the same temperature and velocity
 21 conditions. In Figure 10, Setup II produced more than twice the flux of that from Setup I at the
 22 same temperature, although temperature polarisation of the hot feed in Setup I was theoretically less
 23 than that in Setup II (much higher velocity in Setup I than that in Setup II). Therefore, the reason for
 24 this phenomenon can be explained by the asymmetrical structure of the hollow fibre. According to
 25 [29], the resistance of composite membranes can be represented by:

$$26 R_{membrane} = R_{skin} + R_{principle} = \frac{1}{C_{skin}} + \frac{1}{C_{principle}} \quad (20)$$

27 Combining with Eq. (4)

$$28 \frac{R_{principle}}{R_{skin}} = \frac{C_{skin}}{C_{principle}} = \frac{r_{skin}^a \varepsilon_{skin}}{d_{so} \ln(d_{so}/d_{si}) t_{skin}} \frac{d_{po} \ln(d_{po}/d_{pi}) t_{principle}}{r_{principle}^a \varepsilon_{principle}} \quad (21)$$

$$= \frac{r_{skin}^a}{r_{principle}^a} \frac{V_{skin}}{V_{principle}} \frac{(d_{po}^2 - d_{pi}^2)}{(d_{so}^2 - d_{si}^2)} \frac{d_{po} \ln(d_{po}/d_{pi}) t_{principle}}{d_{so} \ln(d_{so}/d_{si}) t_{skin}}$$

29 where $R_{membrane}$, R_{skin} and $R_{principle}$ are the resistance of membrane, skin layer and principle layer,
 30 C_{skin} and $C_{principle}$ are the mass transfer coefficients of skin layer and principle layer, d_{so} and d_{si} are
 31 the outer and inner diameters of the skin layer, d_{po} and d_{pi} are the outer and inner diameter of the
 32 principle layers, and V_{skin} and $V_{principle}$ are cumulative pore volumes of pore size ranges respectively
 33 in skin layer and principle layer.

34 4.2.2 Heat transfer resistance analysis

35
 36
 37 Based on the data listed in Table 4 and using Eq. (21), it can be estimated that the resistance of the
 38 skin layer is about 1-140 times that of principle layer, depending on the value of a .

39 According to Eq. (5), the heat transfer can be represented,

$$40 Q = H_{latent} N_{skin} + \frac{2\lambda_{skin}}{d_{so} \ln(d_{so}/d_{si})} (T_1' - T') = H_{latent} N_{principle} + \frac{2\lambda_{principle}}{d_{po} \ln(d_{po}/d_{pi})} \quad (22)$$

41 where d_{so} (1670 μm) \approx d_{po} (1665 μm)

42 So,

1 $N_{principle} \approx N_{skin}$, and

$$2 \frac{(T'_1 - T')}{(T' - T'_2)} = \frac{\lambda_{principle} d_{so} \ln(d_{so} / d_{si})}{d_{po} \ln(d_{po} / d_{pi}) \lambda_{skin}} \quad (23)$$

3 Assuming the skin layer and principle layer are prepared from the same material, based on Eq. (6)
 4 and the parameters of each layer are:

$$5 \frac{(T'_1 - T')}{(T' - T'_2)} < \frac{1}{190} \quad (24)$$

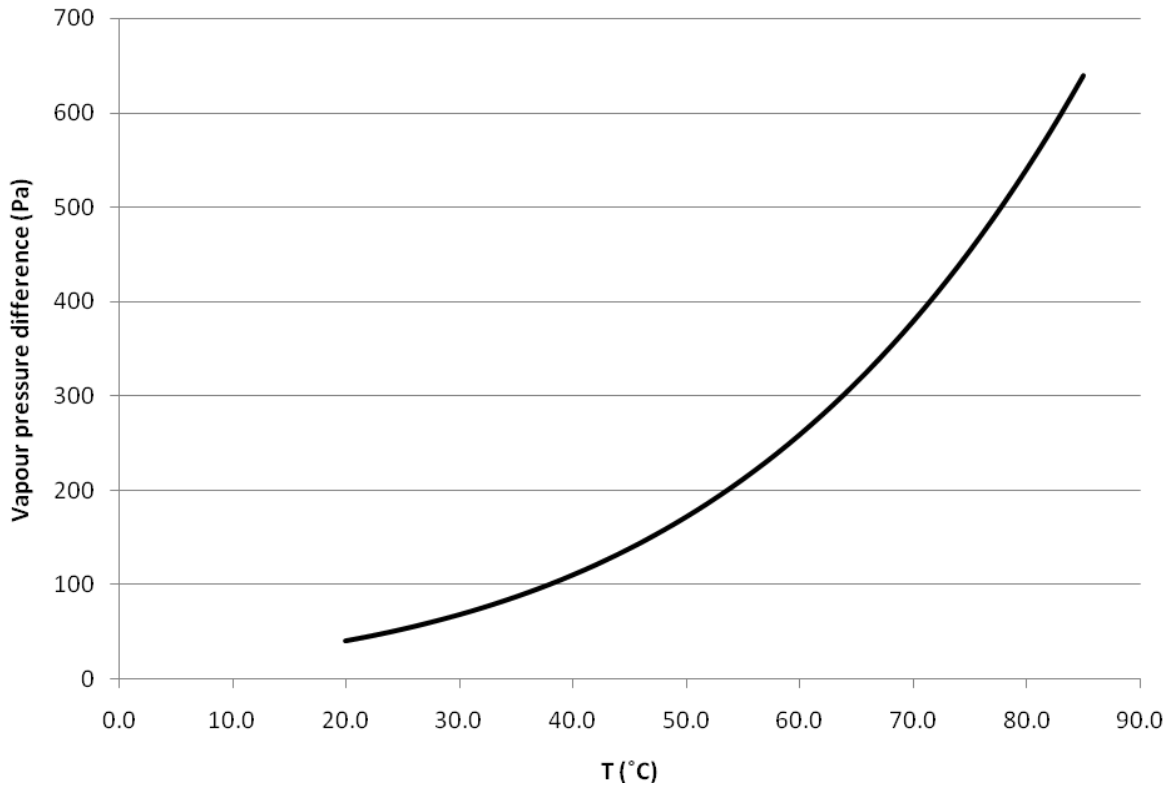
6 because

$$7 |T'_1 - T'_2| > |T' - T'_2| \quad (25)$$

8 Derived

$$9 |T'_1 - T'| < \frac{1}{190} |T'_1 - T'_2| \quad (26)$$

10 In this study, depending upon the velocities, the average ΔT between the hot side and cold side
 11 was 29-35°C at cold and hot inlet temperatures of 20 and 60°C respectively. The largest temperature
 12 difference was 52°C at cold and hot inlet temperatures of 20 and 86°C with a feed flow velocity of
 13 0.4 m/s. Therefore, the theoretical maximum temperature difference across the skin layer is less
 14 than 0.28°C. Figure 14 represents the vapour pressure difference across the skin at a temperature
 15 difference of 0.28°C ($T'_1 < T'$), in which the vapour pressure is given by Antoine equation [30, 31].
 16 From this figure, we find that the vapour pressure difference across the skin layer at $T'_1 = 60^\circ\text{C}$ is 6.2
 17 times of that at $T'_1 = 20^\circ\text{C}$, compared with a flux reduction of 6.2% from the contribution of Knudsen
 18 diffusion coefficient (Eq. 15) in skin layer when T'_1 increased from 20 to 60°C. Thus, if the skin
 19 layer contacts the cold permeate, the vapour pressure across the skin layer will be much smaller
 20 than that when contacting the hot feed. Because the skin layer has greater resistance than the
 21 principle layer, the temperature of the stream contacted with the skin layer will directly affect the
 22 flux of the membrane.



23
 24 Figure 14 Vapour pressure difference across skin layer at different temperatures ($\Delta T = 0.28^\circ\text{C}$)

1 Based on this theory, the bow shaped global mass transfer curve of Setup I in Figure 11 can also
2 be explained. In these experiments, increased velocities reduced both the boundary layer thickness
3 and the surface temperature of the skin layer. At lower velocities (<0.22 m/s), where the boundary
4 layer on cold side is still an important mass transfer barrier, the flux will increase with the thinning
5 of the boundary layer. However, at higher velocities (>0.22 m/s), the resistance of the boundary
6 layer will not change significantly with the increasing velocity and lowering the temperature of the
7 skin layer will reduce the driving force across the skin layer causing a decrease in flux.

8 In comparison, it was also observed that the gradient of Setup III (Figure 11) started to stabilise at
9 velocities higher than 0.22 m/s. In this region, the global mass transfer coefficient increased linearly
10 with velocity in Setup III, while the mass transfer coefficient for Setup I decreased at these
11 velocities. The increase in mass transfer coefficient for Setup III, maybe due to the effect of
12 increasing negative pressure in permeate stream overriding the lower skin temperature.

13 The greatest flux should be achieved when the hot feed is closest to the high mass transfer
14 resistance skin layer and permeate has negative pressure, but this was not attempted because of
15 concerns regarding the collapse of the membrane when under negative pressure on the lumen side.

16 The analysis also showed the mass transfer coefficient to be a better parameter than flux for
17 comparison of MD membranes, as it was less sensitive to the effect of variations in operating
18 temperatures and is therefore more dependent upon material properties.

19 20 **5. Conclusions**

21
22 The performance of asymmetric hollow fibre membranes in DCMD was assessed based on the
23 variation of temperatures, flow velocities, stream configuration and the degree of cold side vacuum
24 pressure in the hollow fibre module. Flux was calculated based on the outside surface area of the
25 hollow fibre membrane, irrespective of the direction of permeate transport as the skin layer had
26 greater influence on mass transfer.

27 The membrane showed different performances when the hot feed passed through different sides
28 (lumen and shell sides) of the membrane. In this study, the highest flux was $19.2 \text{ L.m}^{-2}\text{h}^{-1}$, when the
29 feed flowed through the shell side with a velocity of 0.4 m/s and the inlet temperatures on the cold
30 side and hot side were 20°C and 86°C respectively (without vacuum pressure on the permeate side).
31 The variation in performance can be attributed to the asymmetric structure of the membrane, and
32 the exponential relationship of vapour pressure to temperature.

33 Mass transfer coefficients were calculated to evaluate the performance of the process under
34 different conditions. The use of the mass transfer coefficient removes the temperature dependence
35 of the flux measurements, and so provides a means to study the polarisation effects. This was
36 confirmed by the experimental results which showed that the mass transfer coefficient at high
37 velocities remained approximately constant as the hot feed temperature increased from 30 to 86°C .
38 Therefore, the mass transfer coefficient is a better parameter than flux for comparison of MD
39 membranes, as it is less sensitive to the effect of variations in operating temperatures and is
40 therefore more dependent upon material properties.

41 Negative gauge pressure on the cold side boosted the flux by reducing the pressure within the
42 pores and thereby increasing the rate of mass transfer through the pores. However, the rate of
43 increase in flux reduced at higher vacuum pressures indicating that there is a diminishing return for
44 flux at higher negative pressures beyond -12 kPa (feed velocity >0.22 m/s), due to the skin layer
45 effect.

46 The results show salt rejections higher than 99% can be achieved even at very high volume feed
47 velocities, due to the large ID of the hollow fibre membrane.

1 Acknowledgment

2

3 This work was financially supported by the CSIRO Cluster on Advanced Membrane
4 Technologies for Water Treatment for which we are very grateful.

5 The authors would like to thank Mr. Noel Dow for his assistance in assembling and configuring
6 the equipment used in this work.

7

8 **Nomenclature**

9

a	exponent coefficient of r
A	membrane area
A_{skin}	the cumulative pore surface area of the pore size ranges in skin layer
α_1, α_2	heat transfer coefficient on hot side and cold side
B	geometric factor
b	membrane thickness
$C_{membrane}$	membrane mass transfer coefficient
$C_{skin}, C_{principle}$	the mass transfer coefficients of skin layer and principle layer
d	the mean pore diameter of the membrane
d_o, d_i	outer and inner diameters of the hollow fibre membrane
D_{AB}	the diffusivity of water vapour (A) relative to air (B)
ε	membrane porosity
F	force from surface tension
g	acceleration due to gravity
h	height between the water protrusion and water surface in the beaker
H	water protrusion into the pore
H_{latent}	latent heat of water vaporisation
κ	the mean free path of the transferred gas molecule
λ	thermal conductivity
λ_{air} and λ_{solid}	air thermal conductivity and solid thermal conductivity
Δm	the mass difference
M	the molecular weight of water
N_k, N_m	fluxes contributed by Knudsen and molecule diffusion transition mechanisms
N	vapour flux
P	total gauge pressure in the pore
P_A	partial pressure in the pore
P_f, P_p	gauge pressure of the feed flow and permeate flow
P_{gas}	gas phase pressure in pores
P_{liquid}	pressure of the process liquid
P_{T1}, P_{T2}	vapour pressure at T_1 and T_2
P_{fi}, P_{fo}	vapour pressures at inlet and outlet temperatures of the hot side
P_{pi}, P_{po}	vapour pressures at inlet and outlet temperatures of cold side
ρ	water density
Q_f	feed mass flowrate
r_{max}	the largest pore size of membrane
r	nominal pore size of membrane
R	universal gas constant
$R_{membrane}, R_{skin}, R_{principle}$	resistance of membrane, skin layer and principle layer
θ	contact angle between the solution and the membrane surface

θ'	angle between the water and membrane material
t	pore tortuosity
T	mean temperature in the pore
T_p, T_f	permeate and feed bulk temperatures
T_{fi}, T_{fo}	feed inlet and outlet temperatures
T_1, T_2	feed and permeate temperatures at liquid-vapour interface
T'	temperature between the skin layer and principle layer
T_1' and T_2'	interface temperatures of the pore on on the skin layer side and principle layer side
V_{mass}	mass volume
$V_{skin}, V_{principle}$	cumulative pore volumes of pore size ranges in skin layer and principle layer.
V_{total}	total fibre volume
x_A	mole fraction of water vapour in the pore
γ_l	surface tension of the solution

1

2 Reference

3

- 4 [1] M. C. García-Payo, M. A. Izquierdo-Gil, C. Fernández-Pineda, Wetting Study of Hydrophobic Membranes via
5 Liquid Entry Pressure Measurements with Aqueous Alcohol Solutions, *Journal of Colloid and Interface Science*.
6 230(2000) 420-431.
- 7 [2] J. Phattaranawik, R. Jiratananon, A. G. Fane, Effect of pore size distribution and air flux on mass transport in
8 direct contact membrane distillation, *Journal of Membrane Science*. 215(2003) 75-85.
- 9 [3] L. Martinez-Diez, M. I. Vazquez-Gonzalez, Temperature and concentration polarization in membrane distillation of
10 aqueous salt solutions, *Journal of Membrane Science*. 156(1999) 265-273.
- 11 [4] S. Bonyadi, T. S. Chung, Flux enhancement in membrane distillation by fabrication of dual layer hydrophilic-
12 hydrophobic hollow fiber membranes, *Journal of Membrane Science*. 306(2007) 134-146.
- 13 [5] L.-H. Cheng, P.-C. Wu, J. Chen, Modeling and optimization of hollow fiber DCMD module for desalination, *Journal*
14 *of Membrane Science*. 318(2008) 154-166.
- 15 [6] S. Bonyadi, T.-S. Chung, Highly porous and macrovoid-free PVDF hollow fiber membranes for membrane
16 distillation by a solvent-dope solution co-extrusion approach, *Journal of Membrane Science*. 331(2009) 66-74.
- 17 [7] A. M. Alklaibi, N. Lior, Membrane-distillation desalination: Status and potential, *Desalination*. 171(2005) 111-131.
- 18 [8] Z. Ding, R. Ma, A. G. Fane, A new model for mass transfer in direct contact membrane distillation, *Desalination*.
19 151(2003) 217-227.
- 20 [9] R. W. Schofield, A. G. Fane, C. J. D. Fell, Gas and vapour transport through microporous membranes. I. Knudsen-
21 Poiseuille transition, *Journal of Membrane Science*. 53(1990) 159-171.
- 22 [10] K. W. Lawson, D. R. Lloyd, Membrane distillation, *Journal of Membrane Science*. 124(1997) 1-25.
- 23 [11] J. H. I. Lienhard, J. H. V. Lienhard, *A Heat Transfer Textbook*. 3rd ed., Phlogiston Press, Cambridge,
24 Massachusetts, U.S.A., 2003.
- 25 [12] G. K. Batchelor, *An introduction in fluid dynamics*. First ed., Cambridge University Press, London, 1970.
- 26 [13] L. Ghasemi-Mobarakeh, D. Semnani, M. Morshed, A novel method for porosity measurement of various surface
27 layers of nanofibers mat using image analysis for tissue engineering applications, *Journal of Applied Polymer Science*.
28 106(2007) 2536-2542.
- 29 [14] J. Zhang, N. Dow, M. Duke, E. Ostarcevic, J.-D. Li, S. Gray, Identification of material and physical features of
30 membrane distillation membranes for high performance desalination, *Journal of Membrane Science*. 349(2010) 295-
31 303.
- 32 [15] M. S. Kim, S. J. Lee, J. U. Kang, K. J. Bae, Preparations of Polypropylene Membrane with High Porosity in
33 Supercritical CO₂ and Its Application for PEMFC, *Journal of Industrial and Engineering Chemistry*. 11(2005) 187-193.
- 34 [16] N. Diban, O. C. Voinea, A. Urteaga, I. Ortiz, Vacuum membrane distillation of the main pear aroma compound:
35 Experimental study and mass transfer modeling, *Journal of Membrane Science*. 326(2009) 64-75.
- 36 [17] Z. Wang, Z. Gu, S. Feng, Y. Li, Applications of membrane distillation technology in energy transformation
37 process-basis and prospect, *Chinese Science Bulletin*. 54(2009) 2766-2780.
- 38 [18] M. M. Teoh, T.-S. Chung, Membrane distillation with hydrophobic macrovoid-free PVDF-PTFE hollow fiber
39 membranes, *Separation and Purification Technology*. 66(2009) 229-236.
- 40 [19] D. Li, T.-S. Chung, R. Wang, Morphological aspects and structure control of dual-layer asymmetric hollow fiber
41 membranes formed by a simultaneous co-extrusion approach, *Journal of Membrane Science*. 243(2004) 155-175.
- 42 [20] T. Yanagimoto, Method for manufacture of hollow-fiber porous previous membranes, Japan, (1988)
- 43 [21] M. Matheswaran, T. O. Kwon, J. W. Kim, I. Moon, Factors Affecting Flux and Water Separation Performance in

- 1 Air Gap Membrane Distillation, *Journal of Industrial and Engineering Chemistry*. 13(2007) 965-970.
- 2 [22] M. C. Garcia-Payo, C. A. Rivier, I. W. Marison, U. von Stockar, Separation of binary mixtures by thermostatic
3 sweeping gas membrane distillation: II. Experimental results with aqueous formic acid solutions, *Journal of Membrane*
4 *Science*. 198(2002) 197-210.
- 5 [23] H. Schlichting, K. Gersten, *Boundary-layer theory* 8th ed., Springer, Berlin ; London, 2000.
- 6 [24] J. Phattaranawik, R. Jiratananon, Direct contact membrane distillation: effect of mass transfer on heat transfer,
7 *Journal of Membrane Science*. 188(2001) 137-143.
- 8 [25] T. Y. Cath, V. D. Adams, A. E. Childress, Experimental study of desalination using direct contact membrane
9 distillation: a new approach to flux enhancement, *Journal of Membrane Science*. 228(2004) 5-16.
- 10 [26] C. R. Martinetti, A. E. Childress, T. Y. Cath, High recovery of concentrated RO brines using forward osmosis and
11 membrane distillation, *Journal of Membrane Science*. 331(2009) 31-39.
- 12 [27] T. Y. Cath, S. Gormly, E. G. Beaudry, M. T. Flynn, V. D. Adams, A. E. Childress, Membrane contactor processes
13 for wastewater reclamation in space: Part I. Direct osmotic concentration as pretreatment for reverse osmosis, *Journal of*
14 *Membrane Science*. 257(2005) 85-98.
- 15 [28] Z. Lei, B. Chen, Z. Ding, Membrane distillation, in: Z. Lei, B. Chen, Z. Ding (Z. Lei, B. Chen, Z. Dings), *Special*
16 *Distillation Processes*, Elsevier Science, Amsterdam, 2005, pp. 241-319.
- 17 [29] T. Ahmed, M. J. Semmens, M. A. Voss, Oxygen transfer characteristics of hollow-fiber, composite membranes,
18 *Advances in Environmental Research*. 8(2004) 637-646.
- 19 [30] S. Al-Obaidani, E. Curcio, F. Macedonio, G. Di Profio, H. Al-Hinai, E. Drioli, Potential of membrane distillation in
20 seawater desalination: Thermal efficiency, sensitivity study and cost estimation, *Journal of Membrane Science*.
21 323(2008) 85-98.
- 22 [31] R. C. Reid, J. M. Prausnitz, B. E. Poling, *The properties of gases and liquids*, 1987.
- 23
- 24